Journal of
Synchrotron
Radiation

ISSN 0909-0495

Received 29 July 2010
Accepted 22 January 2011

Quantitative local structure determination in mica crystals: *ab initio* simulations of polarization XANES at the potassium *K*-edge

Wei Xu,[a] Dongliang Chen,[a] Wangsheng Chu,[a] Ziyu Wu,[a,b,c]* Augusto Marcelli,[d,e]* Annibale Mottana,[d,f] Alexander Soldatov[g] and Maria Franca Brigatti[h]

[a]BSRF, Institute of High Energy Physics, Beijing 100049, People's Republic of China, [b]NSRL, University of Science and Technology of China, Hefei 230026, People's Republic of China, [c]Theoretical Physics Center for Science Facilities, Chinese Academy of Sciences, Beijing 100049, People's Republic of China, [d]INFN-LNF, Via E. Fermi 40, 00044 Frascati RM, Italy, [e]University of Science and Technology of China, Chinese Academy of Sciences, Hefei 230026, People's Republic of China, [f]Dipartimento di Scienze Geologiche, Università degli Studi Roma Tre, 00146 Roma, Italy, [g]Center for Nanoscale Structure of Matter, Southern Federal University, 344090 Rostov-on-Don, Russian Federation, and [h]Dipartimento di Scienze della Terra, Università di Modena e Reggio Emilia, 41100 Modena, Italy. E-mail: wuzy@ustc.edu.cn, marcelli@lnf.infn.it

An attempt to refine the local structure of a layered structure such as mica is made by combining angle-resolved XANES (AXANES) and single-crystal X-ray diffraction (SC-XRD) experiments. *Ab initio* calculations of AXANES spectra of several tri-octahedral micas have been used to further interpolate experimental data and to deduce physico/chemical effects. Structural distortions have been found highly correlated with the compositional disordering that arises from electronic interactions between anions and cations, and extend the interlayer entering deep into nearby tetrahedral and octahedral sheets. Multiple occupations at the same atomic site have been investigated in detail both in the parallel and perpendicular components of AXANES spectra. Finally, the best fit obtained, computed in the framework of the multiple-scattering theory, is presented and the limitations of the muffin-tin potential in layered systems are briefly discussed.

Keywords: mica; angle-resolved XANES; layered structure; muffin-tin potentials; multiple-scattering-theory.

1. Introduction

Micas, a widespread group of minerals, have important technological applications for their excellent thermal and electrical properties. They are mainly used as dielectric materials in the electric industry, and as heat-shielding materials in the building and metallurgical industries. In the scientific community micas have other less popular, but highly specialized, uses: for instance, the muscovite mica is a perfect depository matrix for films (Lamelas *et al.*, 1998) or water (Odelius *et al.*, 1997) owing to both its flatness and its very low reactivity. Bent flakes are also used for monochromators and dispersive crystals (Hölzer *et al.*, 1998; Matzuritsky *et al.*, 2001). Micas have been widely used in isotopic geochronology (McDougall & Harrison, 1999) and some particularly ancient mica was even used in the study of the dark matter (Snowden-Ifft *et al.*, 1995).

The mica structure is layered and rather complex (Fig. 1, left panel), representing an interesting research case itself. A preliminary crystal-chemical study of micas can be traced back to the 1930s when Linus Pauling introduced the conceptual pseudo-hexagonal structure model (Pauling, 1930). Later,

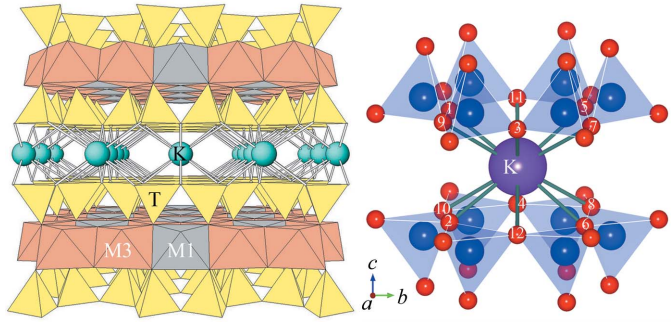

Figure 1
(Left panel) Schematic structure of mica minerals: embedding of one interlayer I in between two TOT layers, each one of which, in turn, consists of one octahedral sheet M sandwiched by two tetrahedral sheets T. (Right panel) The local structure surrounding the K atoms, where 12 O atoms in the first shell are indexed with numbers and connected to the K atom, while the Si atoms locate in the centres of O tetrahedrons.

many works were dedicated to these peculiar minerals. They revealed that the basic structure is made of one layer of cations, I, sandwiched between two ionic blocks, TOT, *viz.* T–M–T. Each block, in turn, is composed of one sheet of octahedra, O or M, in between two sheets of tetrahedra, T. Moreover, the composition of micas was found to be equally complex. The general chemical formula of the mica group is: $AM_{2-3}X_{1-0}T_4O_{10}W_2$, where *A* is the interlayer atom I (*i.e.* K, Na, Rb, Ba, *etc.*), *M* is the atom at the centre of the octahedral sites (*i.e.* Li, Fe^{2+} or Fe^{3+}, Cr, Zn, Mn^{2+} or Mn^{3+}, *etc.*), *T* is the atom set in the tetrahedral sites (*i.e.* Si, Al, Be, Fe^{3+}), *W* refers to anions and anionic groups (*i.e.* Cl, F, OH), O is the oxygen atom, and *X* is a partial octahedral vacancy required to charge balance the multi-valence of certain *M* cations (Rieder *et al.*, 1999).

Furthermore, the low symmetry and multiple occupations of a single atomic site in micas render structural studies interesting but challenging (Brigatti & Guggenheim, 2002). Many structural distortions are present in micas, such as tetrahedral tilting, octahedral contractions, layer flattening, inter-twined distortions, *etc.* (Brigatti *et al.*, 2008). To characterize and finely resolve the local structure of the micas a complex analysis and complementary techniques are required.

X-ray absorption spectroscopy (XAS) (Rehr & Albers, 2000) is, ideally, a local structural probe produced by the scattering of excited photoelectrons. This spectroscopic approach is now popular in many interdisciplinary fields, such as biophysics (Strange & Feiters, 2008), chemical physics (Lee *et al.*, 1981), environmental science and, of course, mineralogy (Mottana, 2004), as in our case. Among the mineralogical community, both types of XAS techniques have been applied (Mottana, 2004) from as early as the 1970s, and became prevailing a few years later. Recently, several systematic investigations on the mica system reflect how applicable this technique has become to minerals. As an element-specific method, XAS spectroscopy had been applied to the *K*-edges of Al (Mottana *et al.*, 1997; Wu *et al.*, 2003) and Si (Tombolini *et al.*, 2002) in the tetrahedral sheet, and to *K*-edges of Fe (Dyar *et al.*, 2001, 2002; Giuli *et al.*, 2001; Tombolini *et al.*, 2002, 2003) and Mg (Tombolini *et al.*, 2003) in the octahedral sheet of micas. In all cases XAS proved profitable, by distinguishing element pairs that X-ray diffraction (XRD) cannot discriminate because of their very small scattering differences. Moreover, XANES has proved its worth in the semi-quantitative evaluation of the expansion of the Mg atom sites in biotite micas (Tombolini *et al.*, 2003) and in the study of the substitution of Cr at different octahedral sites in muscovite micas (Cardelli *et al.*, 2003). The latter study employed the *ab initio* code *MXAN* (Benfatto *et al.*, 2001) to test the different models that would fit the actual structure and obtained remarkably good results.

Previous XANES spectroscopy studies mainly focused on atoms located in the octahedral and tetrahedral sheets. Recently the interest in interlayer atoms was raised owing to the increased brilliance of synchrotron radiation facilities and the upgrading of spectroscopic experimental techniques. By measuring the angle-resolved XANES spectra at the potassium *K*-edge (Cibin *et al.*, 2005, 2006; Marcelli *et al.*, 2006) the local structure around K atoms located in the interlayer can be revealed. Using a statistical method, Brigatti *et al.* (2008) successfully correlated the spectral features in angle-resolved XANES (AXANES) K spectra with structural distances occurring in the interlayer.

The goal of this work is to confirm and improve the reconstruction of the atomic structure of the interlayer of mica (Brigatti *et al.*, 2008) using a different approach. Here, to refine the local structure of potassium in these layered minerals we focus on potassium *K*-edge XANES simulations based on different structural models. In this structural fitting approach we attempted to modify the local symmetry of the basal tetrahedral O atoms while still keeping the crystal symmetry constant so as to maintain the skeleton of the mica lattice.

Different from the octahedral/tetrahedral cations in close-packed structures, the interlayer K atoms locate at open sites, *i.e.* sites with long first-shell bond distances (>2.9 Å) and a highly anisotropic coordination environment. Actually, muffin-tin potentials have serious drawbacks when used in the simulations of open anisotropic structures (Rehr & Albers, 2000), particularly in the near-edge region. The limitations of the muffin-tin potential are also discussed in these layered anisotropic mica structures characterized by large bond distances.

The manuscript will be divided as follows: §1 and §2 briefly introduce the experimental details and background information about angle-resolved XANES spectroscopy; §3 describes the analysis of the polarization spectra; §4 contains the mathematical formalism for decomposing the spectra. Finally, §5 discusses the results while conclusions are summarized in §6.

2. Experimental

The single-crystal sample under study is zinnwaldite (#104 in Brigatti *et al.*, 2000), an intermediate member of the tri-octahedral polylithionite-siderophyllite series. The single-crystal zinnwaldite was obtained from the Pikes Peak granite complex, Colorado, USA, and its single-crystal X-ray diffraction (SC-XRD) high-resolution refinement is available (Brigatti *et al.*, 2000).

Angle-resolved XANES spectra were collected on millimetre-size cleavage flakes at beamline SB3-3 of the Stanford Synchrotron Radiation Laboratory (SSRL), with the SPEAR2 storage ring operating at 3 GeV and current decreasing from 90 to 60 mA, the beam ε vector having >90% linear polarization in the horizontal orbital plane. It is well known that in mica minerals the cleavage plane is parallel to the plane of the interlayer, and cleavage indeed occurs by breaking the weak bonds between the interlayer atoms (mainly K) and the basal O atoms of the two facing tetrahedral sheets. By depositing the cleavage flakes on a flat sample-holder and by rotating this around the [001] direction, angle-resolved XANES spectra were recorded at 15° intervals over a 0–75° range in total electron yield (TEY) mode (Fig. 2). The JUMBO monochromator equipped with InSb crystals cut along (111) gives a

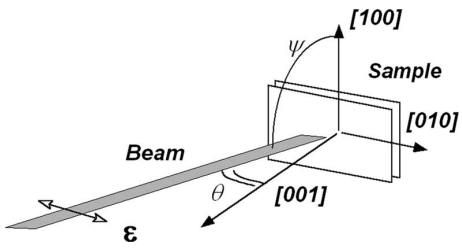

Figure 2
The experimental layout for recording angle-resolved XANES spectra.

resolution of ~1.5 eV in the energy range of the potassium *K*-edge. Energy calibration was performed with reference to the potassium *K*-edge of synthetic KCl (sylvite), repeatedly at regular times. Sylvite was chosen as standard as its spectrum has not only been recorded very precisely (Trischka, 1945) but also calculated *ab initio* equally well (Lavrentyev *et al.*, 1999). All the spectra have been normalized to 50–60 eV above threshold after subtracting the background using a Victoreen polynomial. The set of experimental angle-resolved spectra of zinnwaldite 104 is shown in Fig. 3, and empirical analysis of these spectra can be found elsewhere (Cibin *et al.*, 2006).

3. Angle-resolved XAS spectroscopy and spectral decomposition

Angle-resolved XAS spectroscopy exploits the angular dependence of the absorption cross section in anisotropic systems with symmetry lower than cubic. Through spherical tensor expansion of the absorption cross section, the formula for polarization XANES spectra can be derived with respect to the symmetry of the system and the polarization of the incident beam. The first angular-dependent EXAFS spectra for layered compounds were measured at the Se *K*-edge on synthetic 2*H*-WSe_2 (Heald & Stern, 1977); the high anisotropy of XANES inherent in the system was then pointed out. Later,

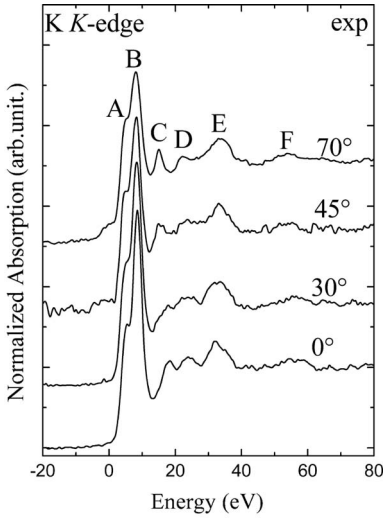

Figure 3
Angle-resolved experimental spectra of zinnwaldite 104 at the *K*-edge of potassium.

Brouder (1990) categorized the polarization dependence for dipolar absorption with respect to the point-group symmetry of the system. In principle, our *C*2 micas would present trichroism. Actually, the layered structure of mica is homogeneous along the plane parallel to the (001) cleavage plane, and exhibits strong anisotropic properties perpendicular to it. Therefore, a dichroic description is also applicable.

The set of angle-resolved XANES spectra was then decomposed into two orthogonal components: in-plane and out-of-plane, using the formula described by Brouder (1990) and the regression fitting procedure proposed by Cibin *et al.* (2006), $\mu(E) = \mu_{\rm par}\sin^2\theta + \mu_{\rm per}\cos^2\theta$, where θ represents the angle between the incident beam and the normal to the crystal plane, and $\mu_{\rm par}$ and $\mu_{\rm per}$ refer to the absorption coefficient in and out of the plane, respectively. The in-plane component refers to a polarization spectrum collected when the electric vector is parallel to the mica *ab* plane, while the out-of-plane component is normal to it, *i.e.* parallel to the mica *c* axis. Hereafter we will indicate the in-plane spectrum as the *XY*-polarized spectrum, and the out-of-plane spectrum that referring to the *Z*-polarization.

4. Calculation details

In order to calculate the polarization spectra and refine the local structure around the K atoms of micas we used the *MXAN* code (Benfatto *et al.*, 2001), whose validity and effectiveness has been demonstrated in both organic (Longa *et al.*, 2001) and inorganic (Monesi *et al.*, 2005) systems. In brief, *MXAN* refines the local structure by searching appropriate potential parameters and changing the geometric position of relevant atoms surrounding the absorber, to minimize the differences between the experimental and the theoretical spectrum. For each step of geometric configuration, theoretical spectra are calculated within the framework of the full-multiple-scattering (FMS) theory (Benfatto *et al.*, 1986) using muffin-tin (MT) partitioned potentials.

Our strategy of calculation is the following. Starting from the X-ray diffraction (XRD) crystal structure (Brigatti *et al.*, 2000) we first selected the cluster size and the maximum orbital angular momentum $l_{\rm max}$ by a convergence criterion, which is achieved by calculating spectra by increasing the cluster size until consecutive clusters produce the same result. The MT radii are selected according to Norman's criteria (Norman, 1974). Calculations including the H atom were performed using the following MT radii: 2.2 Å (K), 0.9 Å (O), 1.0 Å (F), 0.2 Å (H), 1.15 Å (Si), 1.4 Å (Al), 1.2 Å (Fe) and 1.5 Å (Li). According to the Mattheiss prescription (Mattheiss, 1964) an average overlapping factor of ~14% was chosen for the MT approximation. The exchange-correlation potential is accounted for by the energy-independent X-α potential, which performs much better than the Hedin–Lundqvist potential, as implemented in the *MXAN* code. Finally, theoretical spectra are convoluted with a phenomenological Lorentzian function to account for the damping effect (owing to intrinsic and extrinsic losses). The constant part of the function includes the experimental resolution (~1.5 eV)

and the core-hole lifetime (∼0.74 eV at the potassium *K*-edge), while the energy-dependent terms include the onset energy (∼6.18 eV) and a jump ratio (∼4.31) depicting the mean free path (MFP) of photoelectrons used in the standard functional form of solids (Müller *et al.*, 1982).

Some limitations and challenges should be pointed out here. The size convergence is much easier to achieve for *XY*-polarized spectra than for *Z*-polarized spectra. Actually, while the first converges with a 70-atom cluster of size ∼6 Å, the latter does not converge until a cluster of more than 180 atoms extending up to 9 Å is considered. Such a large cluster calculation is rather time-consuming and, at present, represents a challenge for the available computational resources.

Once we determined the cluster size and optimized the potential parameters (MT overlap factor, MFP parameters, Fermi energy, *etc.*), *i.e.* when spectra do not change significantly modifying the parameters of the cluster, we performed a structural fit starting from the initial structure available from SC-XRD data. In our calculation we found that the structural fit significantly modifies spectra. Unphysical results, which sometimes occur when the fit is trapped around a local minimum, have been rejected. To avoid artefacts or unphysical results, we manually performed a consistency calculation, in which we swapped the fitted structure from *XY*- and *Z*-polarization to test whether both spectra can be consistently well reproduced. Finally, we simulated both *XY*- and *Z*-polarized spectra with the same model and with similar potential parameters.

5. Results and discussion

5.1. Size convergence in *XY*- and *Z*-polarization spectra

In Fig. 4 we show the size convergence calculations for the two polarization components of zinnwaldite 104. Using a relatively small cluster (<6 Å, 115 atoms; Fig. 4, left) the calculation of *XY*-polarized spectra easily converges. On the contrary, *Z*-polarized spectra are characterized by larger size effects, *i.e.* a much larger cluster (>8 Å, 179 atoms) has to be considered to achieve convergence (Fig. 4, right). The critical size convergence for the *Z*-polarization is confirmed also by polylithionite and siderophyllite calculations whose clusters were made of 177 and 169 atoms, respectively.

The different size convergence for the two components arises from the large asymmetry of the mica structure, the atoms of which extend through the *XY* plane as periodically spaced as it occurs in normal ionic crystals, whereas sandwiched sheets (*i.e.* tetrahedral and octahedral sheets and interlayer) are crossed along the *Z*-axis. Therefore, the difficulty we encountered is due to the fact that a spherical MT approximation does not adequately describe such a local symmetry along the *Z*-axis as it does along the *XY* plane. We acknowledge that the MT approximation has clear limitations for layered mineral systems such as the micas, and remarkably large clusters are needed when the local symmetry of the system reduces significantly; to improve the convergence of the *Z*-polarized spectra a much larger cluster than the one we used would be required, but this is out of our computational capabilities for the time being.

In the MT approximation the atomic potential is constructed by segregating the space into spherical atomic regions while leaving the interstitial space constant. In a strongly anisotropic layered system such as the micas, the in-plane symmetry is pseudo-hexagonal while the out-of-plane symmetry is reduced to monoclinic owing to the sandwich configuration of the succeeding [T–M–T]–I–[T–M–T] layers (see Fig. 1), *i.e.* a sequence of modules interleaved by I, the interlayer, made up of a single plane of atoms in a planar pseudo-hexagonal configuration. In addition, further anisotropy arises in these [T–M–T] modules because their M sheet is made up of octahedra and their T sheets are made up of tetrahedra. The spherical MT approximation cannot describe properly such a sandwich structure along the *Z*-axis. Thus, in this *Z*-polarization setting, the anistropy of the photoelectron mean free path will affect XANES simulations (Kuzmin, 1994).

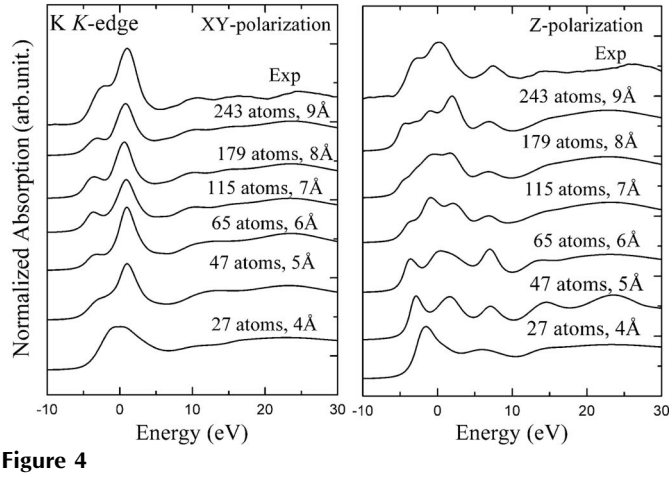

Figure 4
Size convergence calculations for zinnwaldite 104: the *Z*-polarization spectrum (right panel) needs a much larger cluster to converge than the *XY*-polarization spectrum (left panel).

5.2. Tetrahedral substitution: Si *versus* Al

In the ideal structure of micas (Pauling, 1930) the interlayer K atom is coordinated by 12 O atoms in a pseudo-hexagonal setting that are located at distances 2.99–3.26 Å from it, which acts as the central atom, *i.e.* the absorber, in spectroscopic terms. All these O atoms partake in the two tetrahedral layers closest to the interlayer and facing it. The next coordination shell (∼3.76–3.82 Å from the central atom) consists of the 12 Si or Al atoms that centre the tetrahedral sites. Regarding the distribution of these, two rules are to be taken into account: the Loewenstein rule (Loewenstein, 1954) (*i.e.* avoidance of Al–O–Al linkages), and the charge-balance rule (Herrero *et al.*, 1985). The chemical composition of micas requires that the Si and Al atoms occupy the tetrahedral sites with a stoichiometric ratio 3:1, which should be confirmed by SC-XRD refinement. As a matter of fact, in zinnwaldite 104 the T sites

are occupied by Si and Al in the ratio Si:Al = 0.826:0.174 (Brigatti *et al.*, 2000).

To evaluate the influence of multiple occupations we calculated polarized spectra using different clusters where the tetrahedrons facing the interlayer are centred either by Si or by Al. Previously, Brigatti *et al.* (2008) pointed out that the intensity of the main peak (and also that of the shoulder) of their extrapolated experimental *XY*-polarized spectrum is significantly correlated with the Al–Si substitution. Their finding agrees well with our calculated *XY*-polarized spectrum (Fig. 5, left) by the shape of the spectrum from 10 eV below the edge to ∼10 eV above the edge. Upon substitution, only the intensity of the main peak of the Al-100% model decreases with respect to that of the Si-100% model (Fig. 5, left).

On the other hand, when aligning the multiple-scattering (MS) region (Fig. 5, from E to F), remarkable energy shifts are found in the near-edge region and in the intermediate MS region (Fig. 5, from A to D, see arrows). Conventionally, one might align the edge region and interpret the energy shift of the single-scattering contributions according to Natoli's rule, thus assuming them to be the result of bond length differences. However, the MS region of all micas is dominated by the first-shell scattering, and we considered the same first-shell coordination in both models. Therefore, we rather assume that it is this region that should be kept constant when comparing all different model clusters. If this is so, it then becomes clear that peaks are well aligned from higher to lower energy (see F and E) until D is reached. By contrast, peaks in the pre-edge region, such as shoulder A (owing to hybridization), and the near-edge region, such as the white-line B and feature C [marking the projected density of states and the FMS regime (Ankudinov *et al.*, 1998)], are the peaks that can change significantly when the tetrahedral atoms differ. Indeed, a substitution at this site would alter effectively the electronic structure and the MS region contributing to the *Z*-polarized spectrum. The present comparison clearly shows that both the *XY*- and *Z*-polarized spectra are sensitive to tetrahedral substitutions, and the latter spectrum, in particular, is severely dependent on it as a result of the strong anisotropy of the mica system. Judging from the shapes of the calculated spectra and considering the Si:Al stoichiometric ratio, we selected the Si-centred tetrahedral model to perform further calculations.

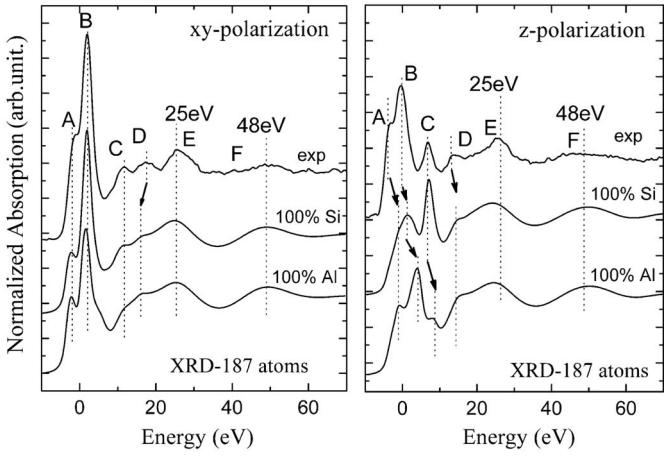

Figure 5
Tetrahedral distribution of Si *versus* Al: comparison of the zinnwaldite 104 simulated spectra under different configurations with the experimental spectrum. Peaks E and F in both simulated and experimental spectra are aligned together.

5.3. Octahedral substitution: Li *versus* Fe

While there is a fixed stoichiometric ratio requirement for the partitioning of Al and Si at the tetrahedral sites, Li and Fe atoms are distributed among the three octahedral sites of the mica structure according to a ratio that is never fixed, but rather loose. This is due to the chemical complexity of the octahedral sheet itself, which can host many cations with different valence, thus also requiring vacancies to balance the sheet charge. This subject deserves deeper consideration, as it affects our calculation models.

In mica, the tetrahedron consists of a central metal atom (Al or Si) and four O atoms at the corners: three 'basal' O atoms (O1, O2 and O3 sites) link the tetrahedral sites on a plane, while the fourth 'apical' (O4 site) O atom of all tetrahedra points toward the octahedral sheet. In our case the 'apical' O4 site may be occupied by O, OH and F anions in different ratios (Brigatti *et al.*, 2000). According to the position of the cations with respect to the O4 anion, there are three independent octahedral sites, named M1, M2 and M3. A regular octahedron has three pairs of point symmetric sites around its centre. When such point symmetric sites are occupied, the central atom is either at the so-called '*trans*' site, *i.e.* the M1 site, or it is in a '*cis*' orientation, and the point symmetric M2 and M3 sites are occupied by different atoms (Mottana *et al.*, 1997). These octahedral configurations directly affect the setting of the tetrahedral sheet (by either tilting or flattening), thus introducing an additional local distortion to the O atoms coordinating the interlayer K atom. According to SC-XRD refinements (Brigatti *et al.*, 2000) the octahedral M1 and M3 sites of our micas are occupied by Li/Fe atoms, vacancies and other atoms in various amounts. In zinnwaldite 104, in particular, the occupational ratios of Li to Fe are ∼3:4 and ∼3:2 for the M1 and M3 sites, respectively.

In order to perform calculations in a reasonable time, we need to simplify the model crystal structure by assuming straightforward configurations. Therefore, we constructed several Li/Fe configurations by alternating Li, Fe and vacancies. Four of these configurations consider only cations: $Li_{M1}Fe_{M3}$, $Li_{M3}Fe_{M1}$, $Li_{M1}Li_{M3}$ and $Fe_{M1}Fe_{M3}$; and two others include a vacancy (□) also: $Li_{10M1}\square_{2M1}Fe_{12M3}$ and $Li_{12M1}Fe_{10M3}\square_{2M3}$. All calculations have been performed using only one type of cluster containing 187 atoms having 12 M1, 12 M2 and 12 M3 sites.

Calculations for different configurations are compared in Fig. 6. The *Z*-polarized spectrum (Fig. 6, right panels) is remarkably sensitive to the distribution of Li, Fe and vacancies; by contrast, the *XY*-polarized spectrum (Fig. 6, left panels) is less sensitive to the octahedral distribution at large distances (∼4 Å alongside the *Z*-axis).

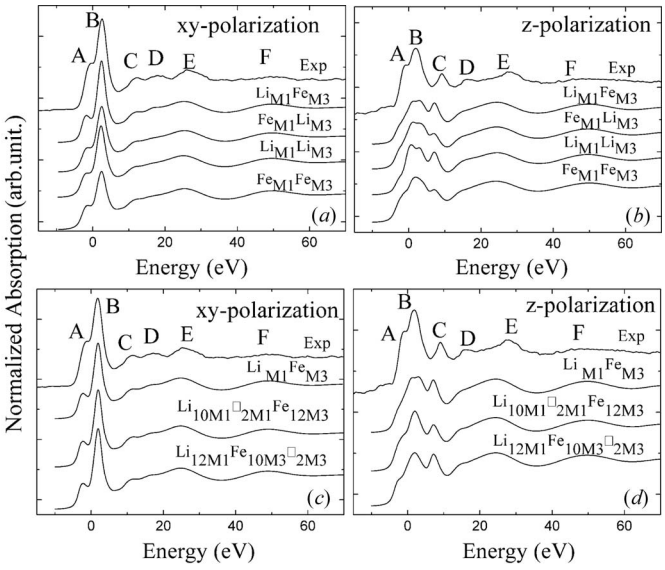

Figure 6
Octahedral distribution of Li, Fe atoms and/or 2/12 vacancies (indicated by □) in different configurations: comparison of the zinnwaldite 104 simulated spectra under different configurations with the experimental spectrum. In the figure $X_{M1}Y_{M3}$ refers to X and Y atoms (or vacancy) occupying the M1 and M3 sites, respectively.

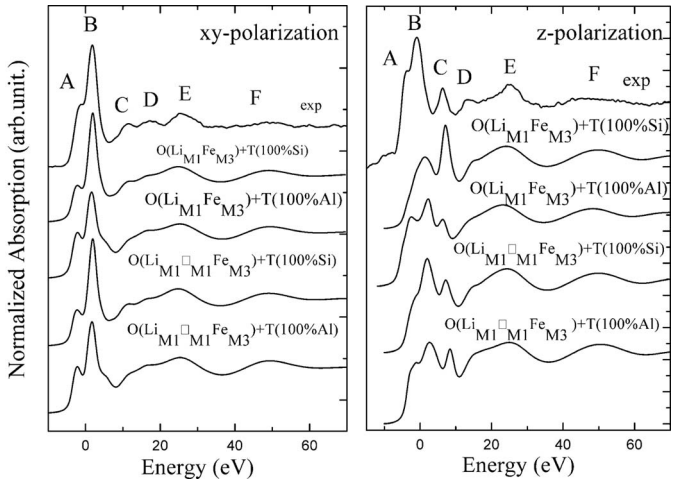

Figure 7
Comparison of the models combining the distribution of the vacancy at the octahedral sites and the Si/Al substitution at the tetrahedral centres with the tetrahedral site Si/Al substitution models. (*a*) $O(Li_{M1}Fe_{M3})$ + T(100% Si); the octahedral M1 and M3 sites are occupied by Li and Fe, respectively, while the tetrahedral sites are occupied only by Si atoms. (*b*) $O(Li_{M1}Fe_{M3})$ + T(100% Al); same Li and Fe distribution at the octahedral sites, while Al replaces for Si in all the tetrahedral sites. (*c*) $O(Li_{M1}\square_{M1}Fe_{M3})$ + T(100% Si); same as model (*a*) but with two vacancies at M1 sites. (*d*) $O(Li_{M1}\square_{M1}Fe_{M3})$ + T(100% Al); same as model (*b*) but with two vacancies at M1 sites.

5.4. Combining tetrahedral Si/Al substitution and the octahedral vacancy distribution

In Fig. 6 it appears clearly that the vacancy model $Li_{10M1}\square_{2M1}Fe_{12M3}$ reproduces the Z-polarized spectra better than other models. In discussing Fig. 5 we have observed already that the tetrahedral Al/Si substitution reproduces well the shoulder A. As a consequence, we combined the above octahedral vacancy distribution and the related tetrahedral substitution in order to test whether a combination of these configurations may reproduce the extrapolated Z-polarized spectra.

In Fig. 7 we compare spectra calculated using models combining the multiple occupations of tetrahedral (Si or Al) and octahedral sites (Fe or Li). In the XY-polarization the tetrahedral Si/Al substitution strongly affects the intensity of the main peak B (decreasing with increasing Al occupation) as well as the pre-edge (increasing with increasing Al occupation), where the calculated differences are mainly due to the electronic structure. On the other hand, the XY-polarization is not sensitive to octahedral distributions [Fig. 7; *cf.* model (*a*) with model (*c*); or model (*b*) with model (*d*)]. Moreover, the simplified model with 100% Si at the nearest tetrahedral centres is the one that reproduces best XY-polarized spectra, at least for the IMS region (*i.e.* 10–30 eV above the edge).

In the Z-polarization the assumed four configurations generate totally different spectral patterns, indicating that this polarization is sensitive not only to the near-range tetrahedral distribution but also to the far-range octahedral distribution. The pre-edge shoulder (10 eV below the edge), the absorption edge and the focusing peak (8 eV above the edge) are all affected by both the tetrahedral Si/Al substitution and the octahedral vacancy distribution. Owing to the above-mentioned limitations of the MT potential along the Z-axis it is not possible to determine a configuration that best matches the Z-polarized spectrum. Moreover, it clearly appears that the near-edge region or the FMS region of Z-polarized mica spectra are significantly affected by the atomic arrangement, *i.e.* by the type and degree of occupation of major atoms occurring up to ∼4.5–6 Å alongside the Z-axis.

5.5. Structural fit using the MT potential

Concerning all structural distortions induced by tetrahedral/octahedral substitutions, we attempted to perform simulations using the most advanced MT potentials now available in order to obtain structural information on mica samples. Here, we summarize the results of the structural fit of mica structures performed using the advanced *MXAN* code.

To achieve the latter we only fit the atomic positions of the 12 nearest neighbouring O atoms (Fig. 1, right panel), located at the bases of the top and bottom facing tetrahedral sheets, until extracted structures were almost identical, *i.e.* with a discrepancy in the position of ≤ 0.01 Å. The final results of calculations and fitting are summarized in Fig. 8. The XY-polarization is reasonably well reproduced with our potential optimization using as starting data the SC-XRD refined structure (Brigatti *et al.*, 2000). Our theoretical calculations reproduce too, and reasonably well, both the edge peak and the following three MS peaks, although peak intensities are in poor agreement with experimental data in particular for the Z-polarization. The fit of the XY-polarized spectrum was performed simultaneously with that of the Z-polarized spec-

Table 1
Comparison of distances between the central potassium and the 12 nearest neighbouring oxygen atoms as obtained by XRD and XAS fits.

The estimated accuracy of the XANES fit is within 0.02 Å. Owing to the large spectral difference (see text) the statistical χ^2 value of the *XY*- and *Z*-polarizations are 401 and 645, respectively.

Coordination	XRD (Å)	XAS (Å)	Residual (Å)	Coordination	XRD (Å)	XAS (Å)	Residual (Å)
O_1	2.99	2.83 (2)	0.163	O_7	3.15	2.96 (1)	0.196
O_2	2.99	3.10 (8)	−0.114	O_8	3.15	2.85 (0)	0.306
O_3	3.02	3.10 (4)	−0.076	O_9	3.25	3.10 (8)	0.150
O_4	3.02	2.91 (7)	0.111	O_{10}	3.25	3.22 (0)	0.038
O_5	3.03	3.04 (8)	−0.017	O_{11}	3.26	3.23 (5)	0.026
O_6	3.03	3.20 (2)	−0.172	O_{12}	3.26	3.29 (4)	−0.034

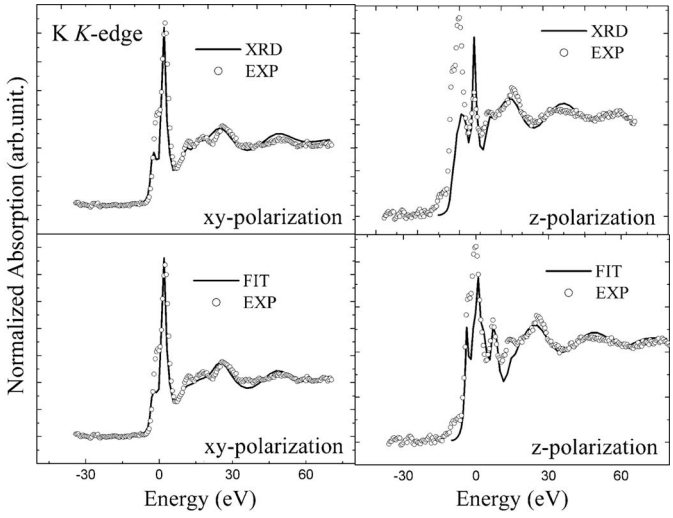

Figure 8
Comparison of experimental polarized spectra and calculations performed with the atomic coordinates refined by SC-XRD (top panels) and by the fit (starting with the SC-XRD refined structure and allowing atomic displacements in the first shell) of the XAS spectra (bottom panels).

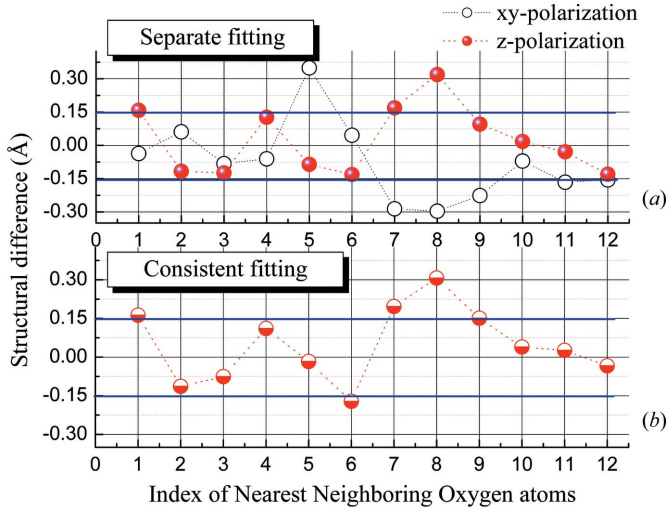

Figure 9
Structural displacements of the K–O nearest neighbouring distances as obtained by the SC-XRD refinement and by (*a*) separate fitting, the independent fit of both *XY*- and *Z*-polarized spectra, and (*b*) consistent fitting, consistent structure that fit best both *XY*- and *Z*-polarized spectra.

trum. After fitting the structure of each spectrum we used the results as the new starting structure for the polarized spectra. By repeating this process several times we eventually achieved a consistent fit. The final *XY*-polarized spectra (Fig. 8, left panels) are in good agreement with the experimental ones, and many features in the *Z*-polarized spectra (Fig. 8, right panels) are also satisfactorily reproduced. These results suggest that the fit, which corresponds to the converged structure achieved by the *MXAN* fitting processes, matches well the real structure.

Comparisons of structural differences between the O atomic positions around K as determined by the SC-XRD refinement and as returned by *MXAN* calculations are shown in Fig. 9. Initially, when both *XY*- and *Z*-polarizations are separately fit, the results clearly show different trends (Fig. 9, top panel) and displacements >0.3 Å, that confirm the strong anisotropy of the mica system. Using the fit strategy outlined above, we obtained a much more consistent result (Fig. 9, bottom panel) and structural distortions clearly emerge. Nevertheless, owing to the shortcomings of the MT potential in the *Z*-polarization and the multiple occupations at the same site, at present the achieved fitting results (see Table 1) are still inadequate and, as an example, not comparable with those achieved for example in other complex systems such as metalloproteins (Yang *et al.*, 2008).

6. Conclusions

We calculated polarized spectra of micas at the potassium *K*-edge using the MT potential in the framework of the MS theory. A rather large atomic cluster (>180 atoms) has been employed to reproduce in a reasonable way the experimental spectra, in particular to achieve the convergence in both *XY*- and *Z*-polarizations. By adjusting the positions of O atoms in the tetrahedral sheet we were able to obtain a rather good agreement for *XY*- and *Z*-polarized spectra in the EXAFS region (30–80 eV above the edge). Calculations show also that the fit of the polarized XANES spectra (as shown by the fit of the *XY*-polarization) is useful to distinguish between different local structures and to improve the description of complex real structure at the atomic level.

On the contrary, a large discrepancy between theory and experiment is observed in the near-edge region of *Z*-polarized spectra. We point out that this failure is associated with the

limitations of the MT potential when describing open and layered structures along a direction perpendicular to layers (Cibin *et al.*, 2010).

To overcome shortcomings associated with the MT potential, novel techniques based on non-MT potential calculations have to be considered (Hatada *et al.*, 2007; Joly, 2001). However, the use of non-MT methods is still in its infancy. Moreover, at present non-MT calculations are severely limited by both the computing time and available computing resources. Calculations using non-MT full potentials codes (Hatada *et al.*, 2007; Joly, 2001), possibly implemented with advanced algorithms and novel fitting methods (Smolentsev & Soldatov, 2006), should be envisaged to refine these two-dimensional layered structures to a level of accuracy as it is presently possible for three-dimensional highly symmetric structures. In addition to improvements associated with the application of non-MT potentials, micas are systems for which it is really necessary to perform XANES calculations as the average of (many) different local structural configurations. Additional contributions such as vibronic effects (Ankudinov & Rehr, 2005) could occur although their contribution is probably negligible when compared with the effects owing to the MT potential discussed above. Indeed, in micas and in many other silicates the fractional occupations in tetrahedral and octahedral sites as well as the possible presence of vacancies have to be properly considered to describe accurately these complex anisotropic structures. Finally, more sophisticated exchange-correlation potentials (Fujikawa *et al.*, 2000) or other energy-independent X-α potentials would be helpful to improve fitting in the EXAFS region.

This work was partly supported by the National Outstanding Youth Fund (Project No. 10125523 to ZW) and by the Knowledge Innovation Program of the Chinese Academy of Sciences (KJCX2-YW-N42). Our research on micas enjoys the joint support of Italy's Ministero dell' Istruzione Università e Ricerca (MIUR) and of Università degli Studi Roma Tre under projects 'Effect of petrological variables on mica crystal chemistry' (PRIN2004) and 'Micas: cation ordering and anionic composition as petrogenetic control factors' (PRIN2006). We would also like to thank M. Benfatto, K. Hayakawa and H. Hatada for many helpful discussions about the *MXAN* code. Special acknowledgment is due to Y. Joly for helpful instructions regarding the use of the *FDMNES* code. We are also grateful to D. Hampai and M. A. Soldatov for testing FDM calculations over large atomic clusters. We gratefully acknowledge the support of the Italian Ministry Foreign Affairs in the framework of the 12th Executive Programme of Scientific and Technological Cooperation between the Italian Republic and the People's Republic of China.

References

Ankudinov, A. L., Ravel, B., Rehr, J. J. & Conradson, S. D. (1998). *Phys. Rev. B*, **58**, 7565–7576.
Ankudinov, A. L. & Rehr, J. J. (2005). *Phys. Scr.* **115**, 24–27.
Benfatto, M., Congiu-Castellano, A., Daniele, A. & Della Longa, S. (2001). *J. Synchrotron Rad.* **8**, 267–269.
Benfatto, M., Natoli, C. R., Bianconi, A., Garcia, J., Marcelli, A., Fanfoni, M. & Davoli, I. (1986). *Phys. Rev. B*, **34**, 5774–5781.
Brigatti, M. F. & Guggenheim, S. (2002). Editors. *Mica Crystal Chemistry and the Influence of Pressure, Temperature and Solid Solution on Atomistic Models.* Chantilly: Mineralogical Society of America.
Brigatti, M. F., Lugli, C., Poppi, L., Foord, E. E. & Kile, D. E. (2000). *Am. Mineral.* **85**, 1275–1286.
Brigatti, M. F., Malferrari, D., Poppi, M., Mottana, A., Cibin, G., Marcelli, A. & Cinque, G. (2008). *Am. Mineral.* **93**, 821–830.
Brouder, C. (1990). *J. Phys. Condens. Matter*, **2**, 701–738.
Cardelli, A., Cibin, G., Benfatto, M., Della Longa, S., Brigatti, M. F. & Marcelli, A. (2003). *Phys. Chem. Miner.* **30**, 54–58.
Cibin, G., Mottana, A., Marcelli, A. & Brigatti, M. F. (2005). *Mineral. Petrol.* **85**, 67–87.
Cibin, G., Mottana, A., Marcelli, A. & Brigatti, M. F. (2006). *Am. Mineral.* **91**, 1150–1162.
Cibin, G., Mottana, A., Marcelli, A., Cinque, G., Xu, W., Wu, Z. & Brigatti, M. F. (2010). *Am. Mineral.* **95**, 1084–1094.
Della Longa, S., Arcovito, A., Girasole, M., Hazemann, J. L. & Benfatto, M. (2001). *Phys. Rev. Lett.* **87**, 155501.
Dyar, M. D., Delaney, J. S. & Sutton, S. R. (2001). *Eur. J. Mineral.* **13**, 1079–1098.
Dyar, M. D., Lowe, E. W., Guidotti, C. V. & Delaney, J. S. (2002). *Am. Mineral.* **87**, 514–522.
Fujikawa, T., Hatada, K. & Hedin, L. (2000). *Phys. Rev. B*, **62**, 5387–5398.
Giuli, G., Paris, E., Wu, Z. Y., Brigatti, M. F., Cibin, G., Mottana, A. & Marcelli, A. (2001). *Eur. J. Mineral.* **13**, 1099–1108.
Hatada, K., Hayakawa, K., Benfatto, M. & Natoli, C. R. (2007). *Phys. Rev. B*, **76**, 060102.
Heald, S. M. & Stern, E. A. (1977). *Phys. Rev. B*, **16**, 5549–5559.
Herrero, C. P., Sanz, J. & Serratosa, J. M. (1985). *J. Phys. C*, **18**, 13–22.
Hölzer, G., Wehrhan, O., Heinisch, J., Förster, E., Pikuz, T. A., Faenov, A. Y., Pikuz, S. A., Romanova, V. M. & Shelkovenko, T. A. (1998). *Phys. Scr.* **57**, 301–309.
Joly, Y. (2001). *Phys. Rev. B*, **63**, 125120–125130.
Kuzmin, A. (1994). *J. Phys. Condens. Matter*, **6**, 5761–5770.
Lamelas, F. J., Schmidt, J. D. & Xiong, M. (1998). *Phys. Rev. B*, **58**, 14270–14278.
Lavrentyev, A. A., Gabrelian, B. V., Nikiforov, I. Y. & Rehr, J. J. (1999). *J. Phys. Chem. Solids*, **60**, 787–790.
Lee, P. A., Citrin, P. H., Eisenberger, P. & Kincaid, B. M. (1981). *Rev. Mod. Phys.* **53**, 769–806.
Loewenstein, W. (1954). *Am. Mineral.* **39**, 92–96.
McDougall, I. & Harrison, T. M. (1999). *Geochronology and Thermochronology by the 40Ar/39Ar Method*, 2nd ed. Oxford: Oxford University Press.
Marcelli, A., Cibin, G., Cinque, G., Mottana, A. & Brigatti, M. F. (2006). *Radiat. Phys. Chem.* **75**, 1596–1607.
Mattheiss, L. F. (1964). *Phys. Rev.* **133**, A1399–A1403.
Matzuritsky, M. I., Soldatov, A. V., Lyashenko, V. L., Latush, E. M., Kozakov, A. T., Shevtsova, S. I. & Marcelli, A. (2001). *Tech. Phys. Lett.* **27**, 11.
Monesi, C., Meneghini, C., Bardelli, F., Benfatto, M., Mobilio, S., Manju, U. & Sarma, D. D. (2005). *Phys. Rev. B*, **72**, 174104.
Mottana, A. (2004). *EMU Notes in Mineralogy*, Vol. 6, *Spectroscopic Methods in Mineralogy*, edited by A. Beran and E. Libowitzky, pp. 1–95. European Mineralogical Union.
Mottana, A., Robert, J.-L., Marcelli, A., Giuli, G., Della Ventura, G., Paris, E. & Wu, Z. (1997). *Am. Mineral.* **82**, 497–502.
Müller, J. E., Jepsen, O. & Wilkins, J. W. (1982). *Solid State Commun.* **42**, 365–368.
Norman, J. G. (1974). *Mol. Phys.* **81**, 1191–1198.
Odelius, M., Bernasconi, M. & Parrinello, M. (1997). *Phys. Rev. Lett.* **78**, 2855–2858.
Pauling, L. (1930). *Proc. Natl Acad. Sci.* **16**, 123–129.
Rehr, J. J. & Albers, R. C. (2000). *Rev. Mod. Phys.* **72**, 621–654.

Rieder, M., Cavazzini, G., D'Yakonov, Y. S., Frank-Kamenetskii, V. A., Gottardi, G., Guggenheim, S., Koval, P. V., Müeller, G., Neiva, A. M. R., Radoslovich, E. W., Robert, J. L., Sassi, F. P., Takeda, H., Weiss, Z. & Wones, D. R. (1999). *Mineral. Mag.* **63**, 267–279.
Smolentsev, G. & Soldatov, A. (2006). *J. Synchrotron Rad.* **13**, 19–29.
Snowden-Ifft, D. P., Freeman, E. S. & Price, P. B. (1995). *Phys. Rev. Lett.* **74**, 4133–4136.
Strange, R. W. & Feiters, M. C. (2008). *Curr. Opin. Struct. Biol.* **18**, 609–616.
Tombolini, F., Cibin, G., Marcelli, A., Mottana, A., Brigatti, M. F. & Giuli, G. (2003). *X-ray and Inner-Shell Processes*, pp. 481–490. Rome: AIP.
Tombolini, F., Marcelli, A., Mottana, A., Cibin, G., Brigatti, M. F. & Giuli, G. (2002). *Int. J. Mod. Phys. B*, **16**, 1673–1679.
Trischka, J. W. (1945). *Phys. Rev.* **67**, 318–320.
Wu, Z. Y., Marcelli, A., Cibin, G., Mottana, A. & Della Ventura, G. (2003). *J. Phys. Condens. Matter*, **15**, 7139–7148.
Yang, F., Chu, W., Yu, M., Wang, Y., Ma, S., Dong, Y. & Wu, Z. (2008). *J. Synchrotron Rad.* **15**, 129–133.